Engineering multiscale hollow core-shell nanostructures via in-situ surface functionalization for advanced electrochemical energy storage applications

Wang Yan[a], Wang Hanbo[a], Xu Yahui[a], Zhu Dongyu[a], Wang Ziming[a], Li Yiduo[a,d], Tian Yumei[a*], Lu Haiyan[a,b,c*]

a College of Chemistry, Jilin University, Changchun, 130012, People's Republic of China.

b College of Chemistry, State Key Laboratory of Inorganic Synthesis and Preparative Chemistry, Key Laboratory of Physics and Technology for Advanced Batteries, Ministry of Education, Jilin University, Changchun 130012, PR China.

c Advanced Energy Systems and Intelligent Detection Technological Innovation University Enterprise Joint Laboratory of Jilin Province, PR China.

d College of Instrumentation and Electrical Engineering, Jilin University, Changchun, 130021, China.

* Indicates co-corresponding author.

Materials and instruments

The following chemical reagents and materials were employed in the course of this investigation. Cobalt nitrate ($Co(NO_3)_2{\cdot}6H_2O$, 99.9 %), nickel nitrate ($Ni(NO_3)_2{\cdot}6H_2O$, 98 %), 2-methylimidazole ($C_4H_6N_2$, 98 %), tannic acid ($C_{76}H_{52}O_{46}$, ACS), cetyltrimethylammonium bromide (CTAB, 99 %), ammonium fluoride (NH_4F, 99.5 %), activated carbon (AC), acetylene carbon black (99.95 %), and polytetrafluoroethylene (PTFE) were purchased from Shanghai Aladdin Biochemical Technology Co., Ltd, China. Ethyl alcohol (C_2H_5OH, 99.8 %), ammonium hydroxide (30 %), and potassium hydroxide (KOH, 98 %) were sourced from Beijing Chemical Works. All chemical reagents were used as received without further purification. Throughout the entire experiment, ultrapure water (resistivity of 18.25 MΩ cm) was employed as the solvent for all chemical reagents.

Scanning electron microscopy (SEM) analysis was conducted using a HITACHI SU020 microscope operating at 3 kV. Transmission electron microscopy (TEM) imaging was performed utilizing a Philips FEI Tecnai G2S-Twin microscope equipped with a field emission gun, operating at 200 kV. The phase structures of the samples were characterized by X-ray diffraction (XRD) using a Rigaku X-ray diffractometer with Cu Kα radiation (λ = 1.54178 Å) at 50.0 kV and 200.0 mA. The diffraction data were recorded in the 2θ range of 5-80° with a scan rate of 5° min^{-1}. Fourier transform infrared (FT-IR) spectra were recorded on a Nicolet 400 Fourier transform infrared spectrometer. Raman analysis was conducted using a Horiba LabRAM HR Evolution spectrometer, with laser excitation at 532 nm. Nitrogen physisorption tests were carried out at 77 K using a QuantachromeAutosorb-IQ-Mplxq instrument. X-ray photoelectron spectra (XPS) were recorded on a Thermo Fisher Scientific ESCALAB 250Xi unit with Al-Kα (1486.6 eV) as the X-ray source. For electrochemical measurement, a CHI660E electrochemical workstation (Shanghai, Chenhua) equipped with a conventional three-electrode system was employed.

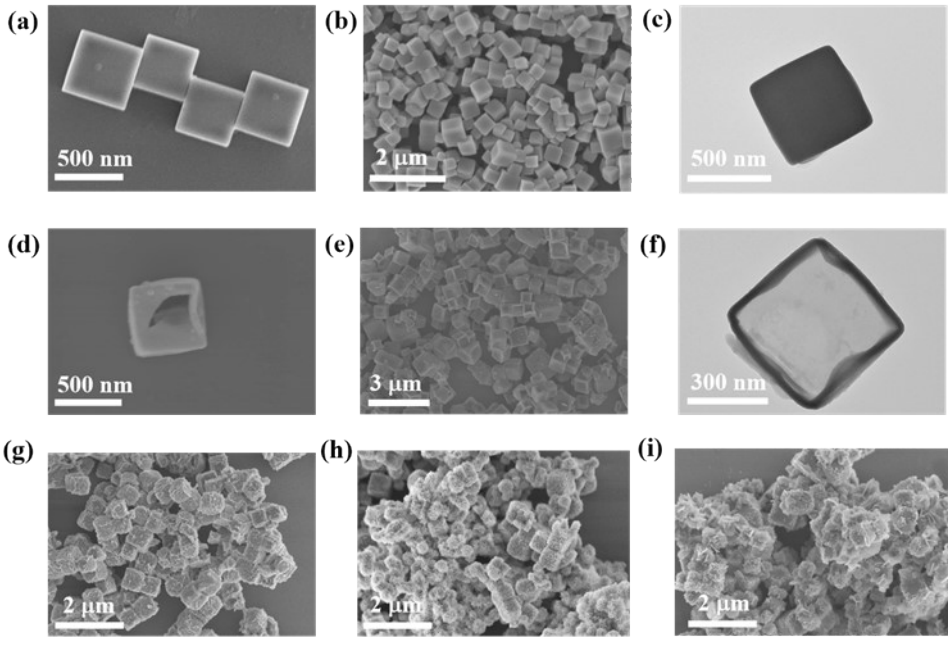

Fig. S1. (a,b) The different-sized SEM images of ZIF-67 NCs; (c) The TEM image of ZIF-67 NCs; (d,e) The different-sized SEM images of HZIF-1.2; (f) The TEM image of HZIF-1.2; (g) The SEM images of Co_3O_4-HNC@NiCo-LDH-0.5 at low magnification; (h) The SEM images of Co_3O_4-HNC@NiCo-LDH-1 at low magnification; (i) The SEM images of Co_3O_4-HNC@NiCo-LDH-2 at low magnification.

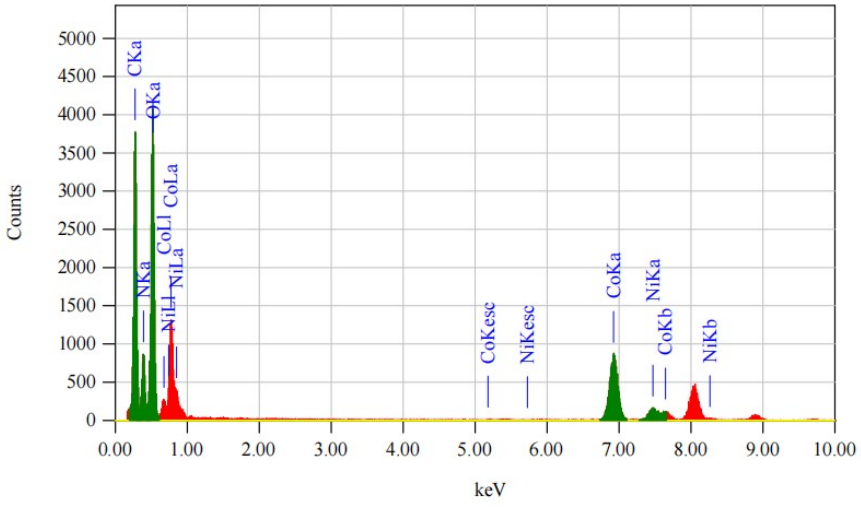

Fig. S2. The Energy spectrum of Co_3O_4-HNC@NiCo-LDH-1.

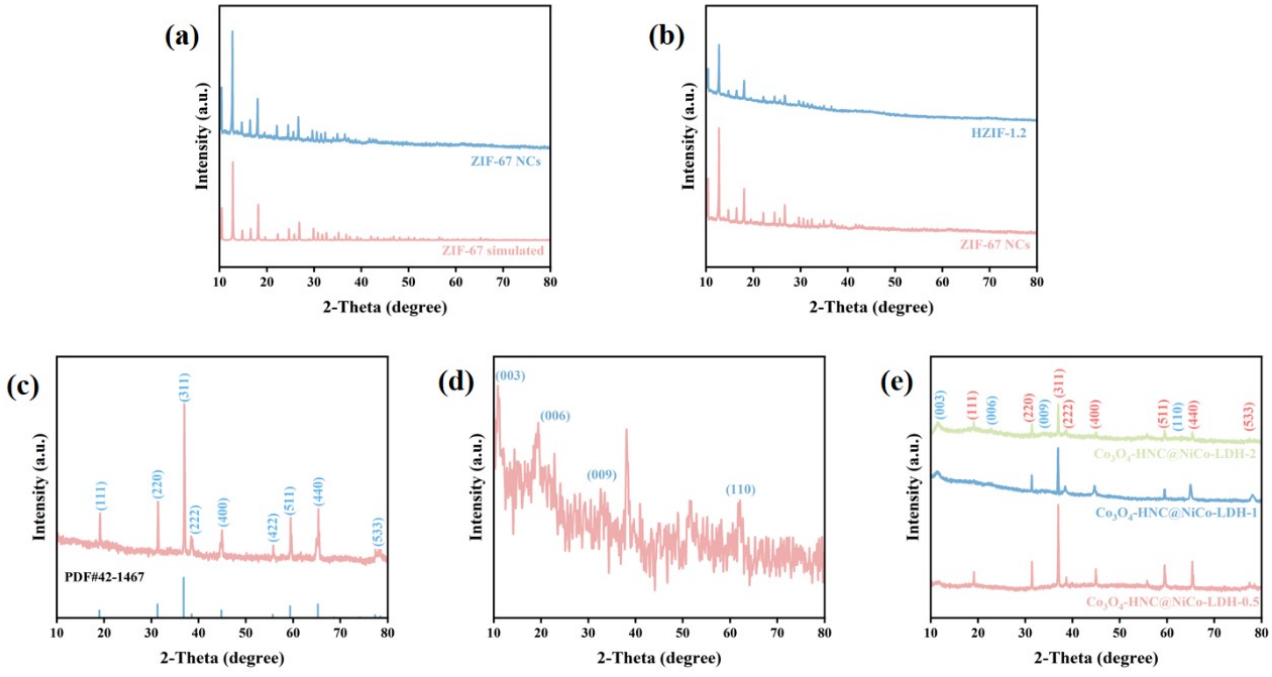

Fig. S3. The XRD patterns of (a) ZIF-67 NCs; (b) HZIF-1.2; (c) Co_3O_4-HNCs; (d) NiCo-LDH; (e) Co_3O_4-HNC@NiCo-LDH.

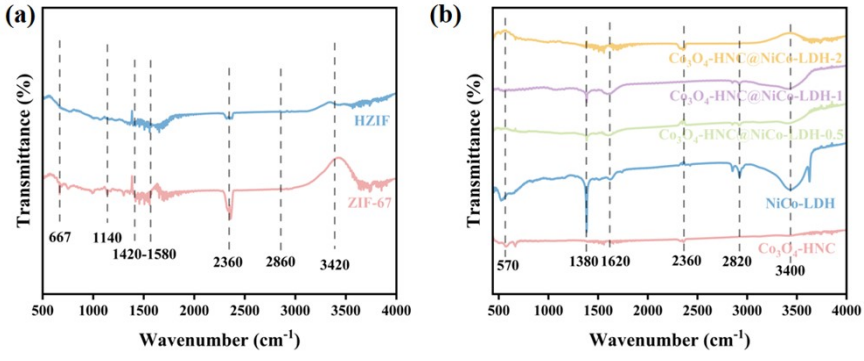

Fig. S4. FT-IR spectra of different samples. (a) ZIF-67 NCs and HZIF-1.2; (b) Co_3O_4-HNCs, NiCo-LDH, Co_3O_4-HNCs, and Co_3O_4-HNCs@NiCo-LDH.

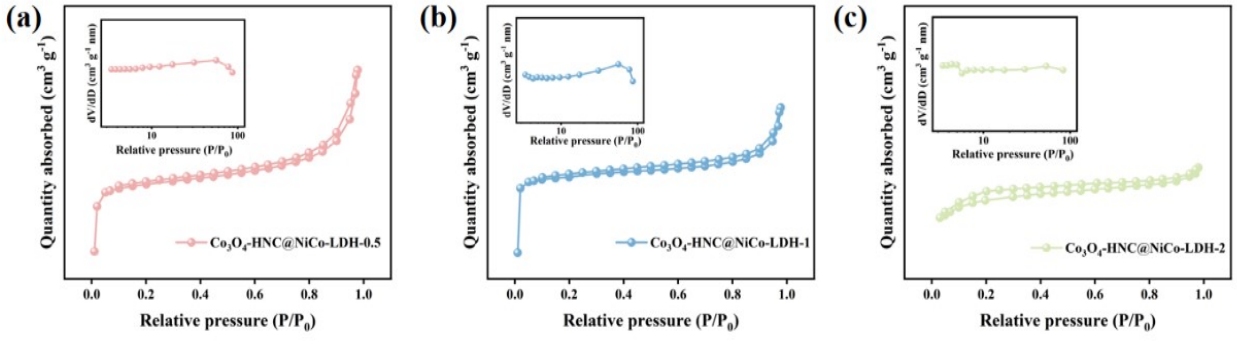

Fig. S5. The N_2 adsorption-desorption isotherm loops and related pore size plots of (a) Co_3O_4-HNC@NiCo-LDH-0.5; (b)Co_3O_4-HNC@NiCo-LDH-1; (c)Co_3O_4-HNC@NiCo-LDH-2.

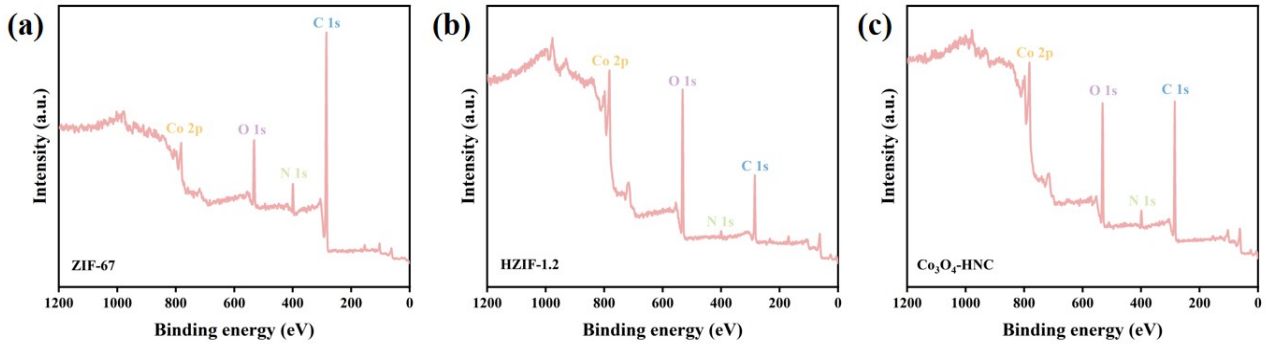

Fig. S6. The XPS survey spectra of (a) ZIF-67 NCs; (b) HZIF-1.2; (c) Co_3O_4-HNCs.

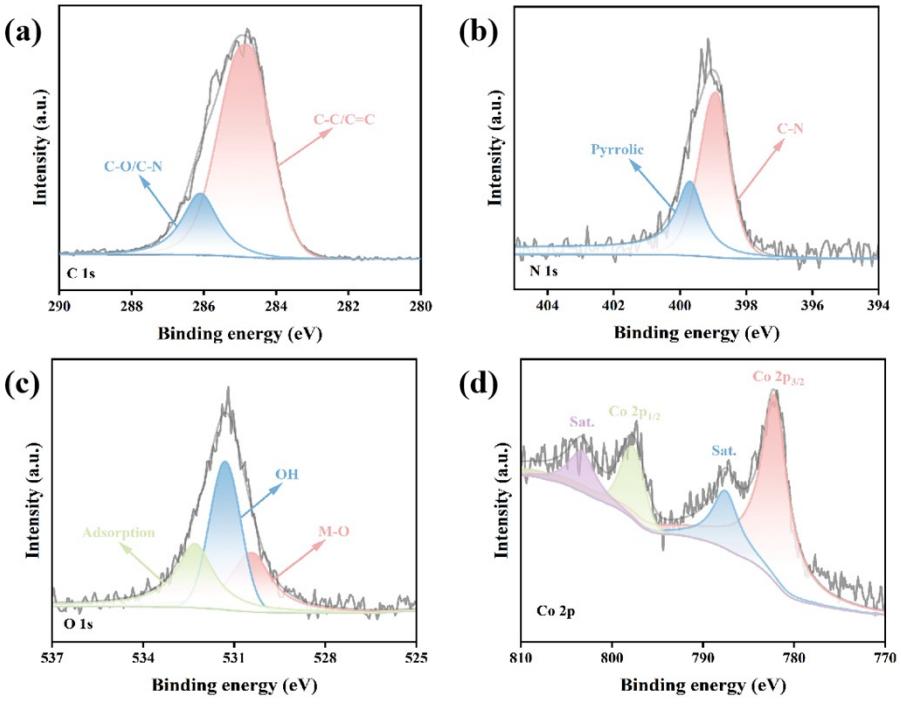

Fig. S7. (a-d) C 1s, N 1s, O 1s, and Co 2p spectra of the ZIF-67 NCs.

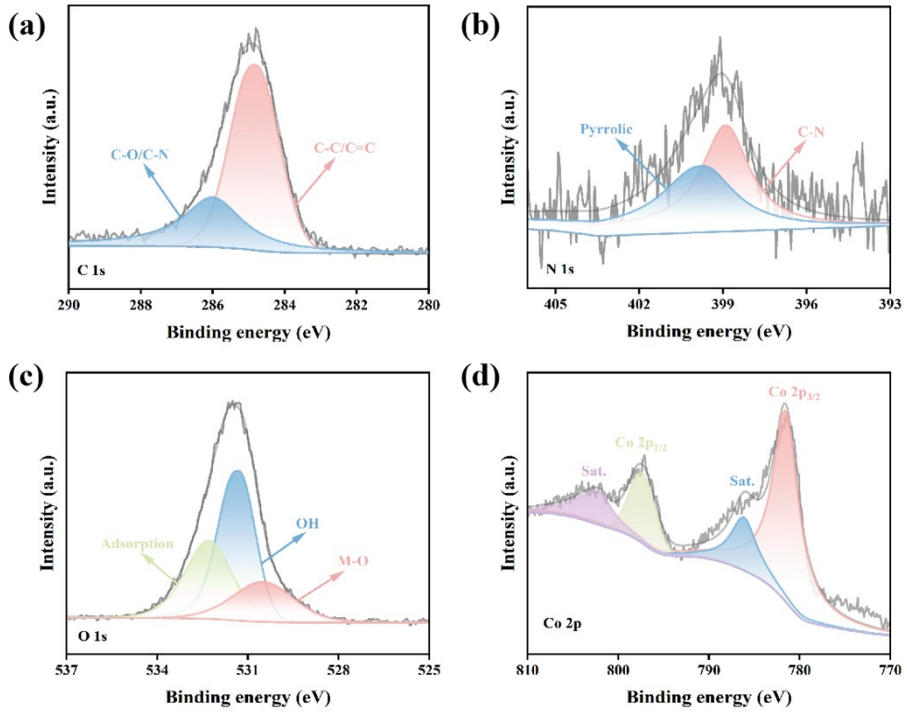

Fig. S8. (a-d) C 1s, N 1s, O 1s, and Co 2p spectra of the HZIF-1.2.

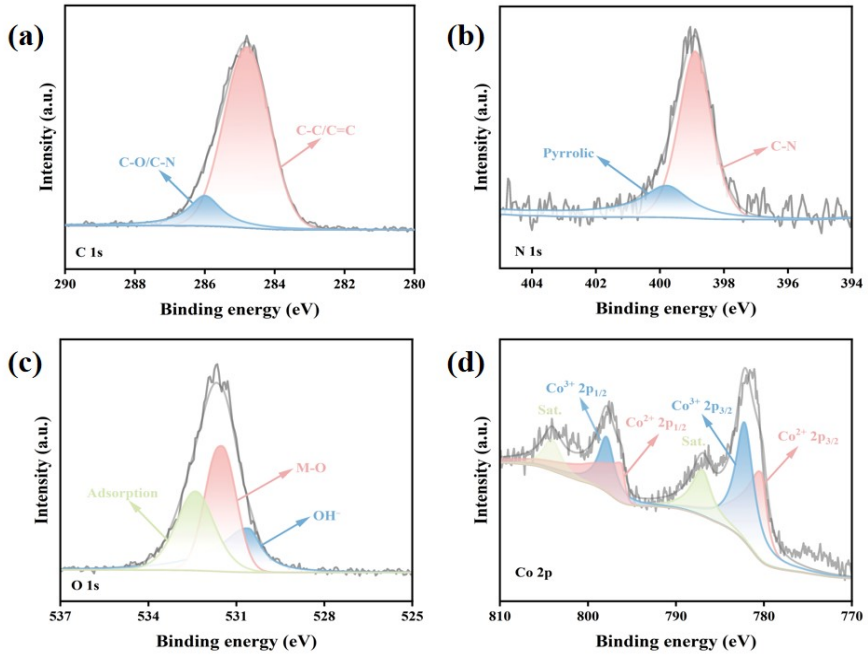

Fig. S9. (a-d) C 1s, N 1s, O 1s , and Co 2p spectra of the Co_3O_4-HNCs.

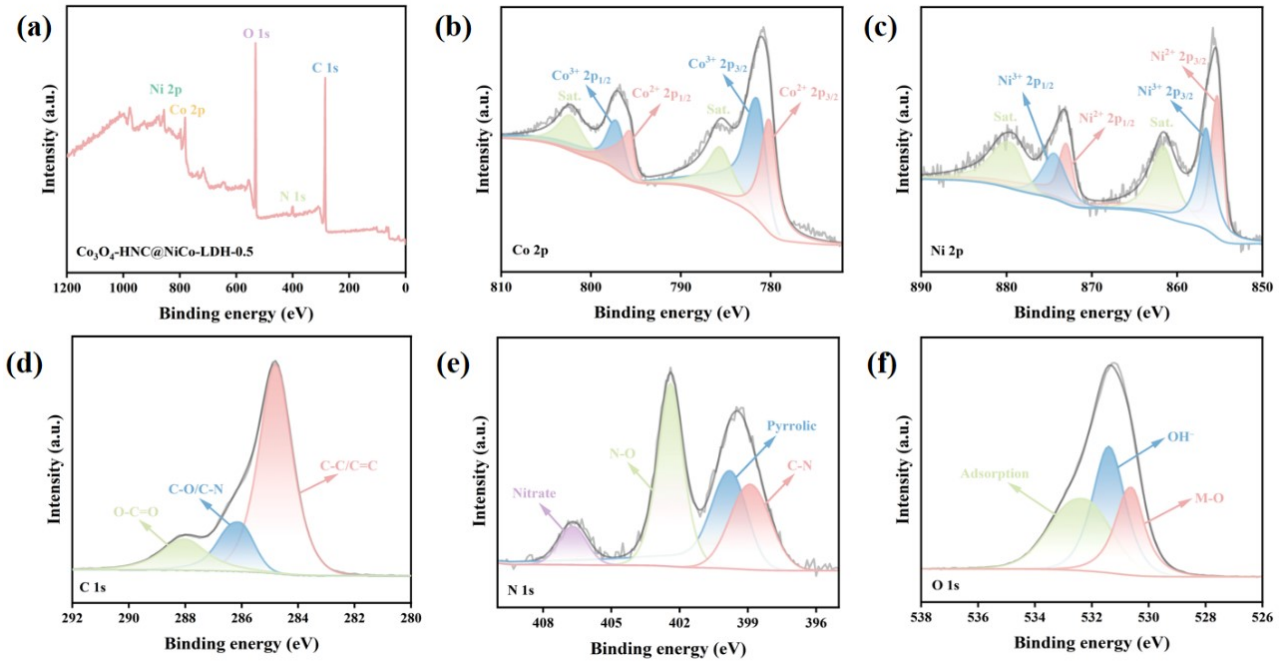

Fig. S10. (a) XPS survey spectra of the composites Co_3O_4-HNC@NiCo-LDH-0.5; (c-f) Co 2p, Ni 2p, C 1s, N 1s, and O 1s spectra of the composites Co_3O_4-HNC@NiCo-LDH-0.5.

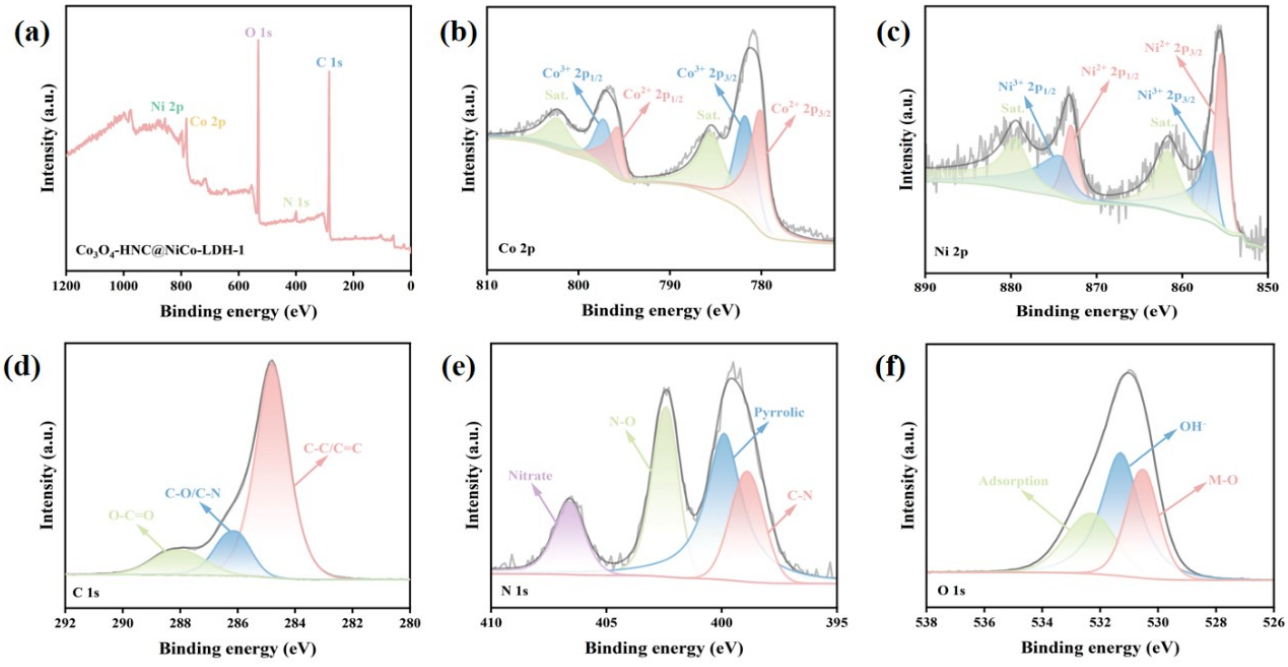

Fig. S11. (a) XPS survey spectra of the composites Co_3O_4-HNC@NiCo-LDH-1; (c-f) Co 2p, Ni 2p, C 1s, N 1s, and O 1s spectra of the composites Co_3O_4-HNC@NiCo-LDH-1.

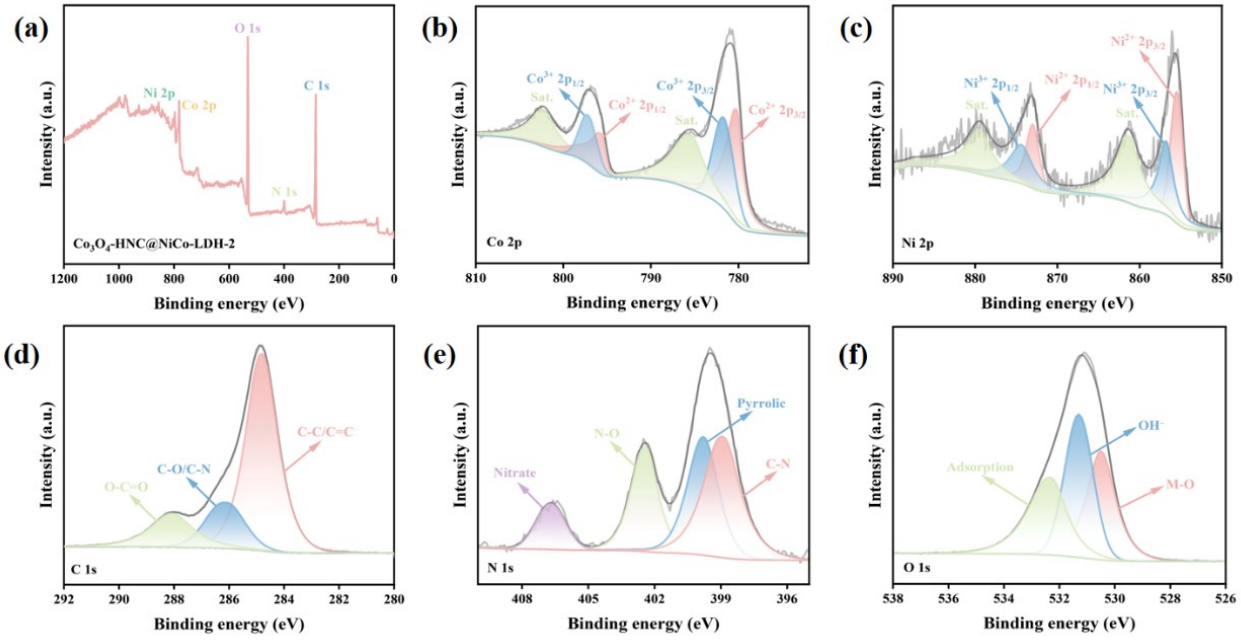

Fig. S12. (a) XPS survey spectra of the composites Co_3O_4-HNC@NiCo-LDH-2; (c-f) Co 2p, Ni 2p, C 1s, N 1s, and O 1s spectra of the composites Co_3O_4-HNC@NiCo-LDH-2.

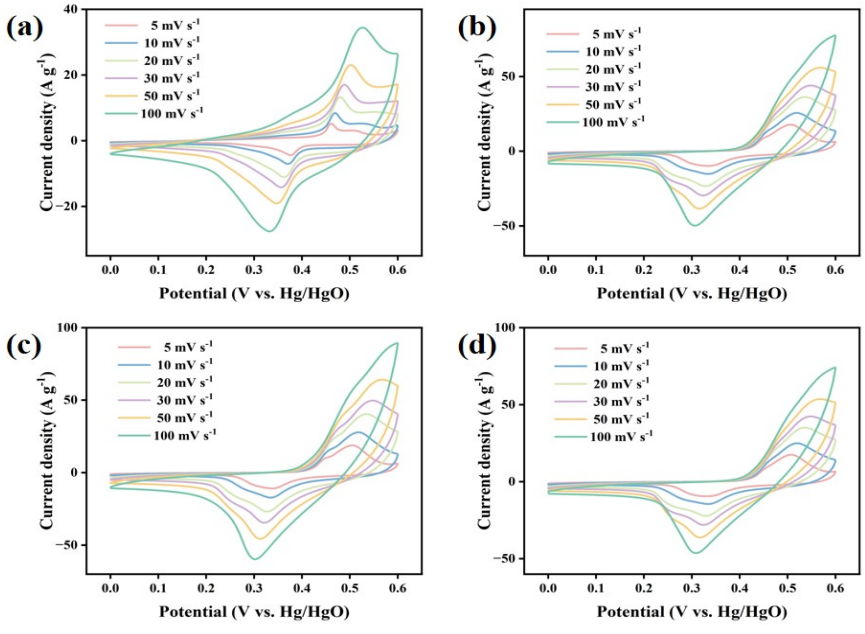

Fig. S13. CV of the (a) ZIF-67 NCs; (b) HZIF-0.9; (c) HZIF-1.2; (D) HZIF-1.5 at different scan rates.

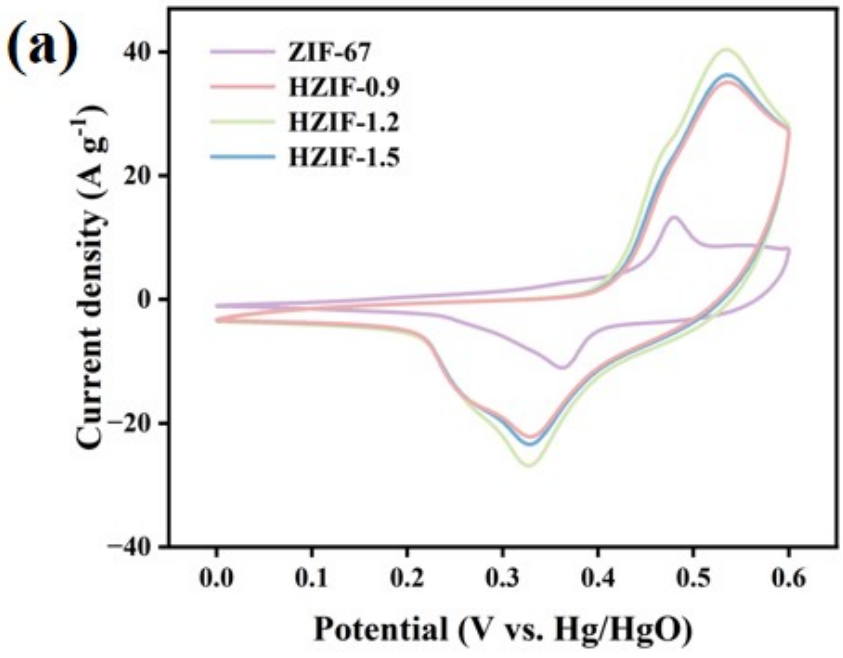

Fig. S14. Comparison of CV curves at a scan rate of 20 mV s^{-1}.

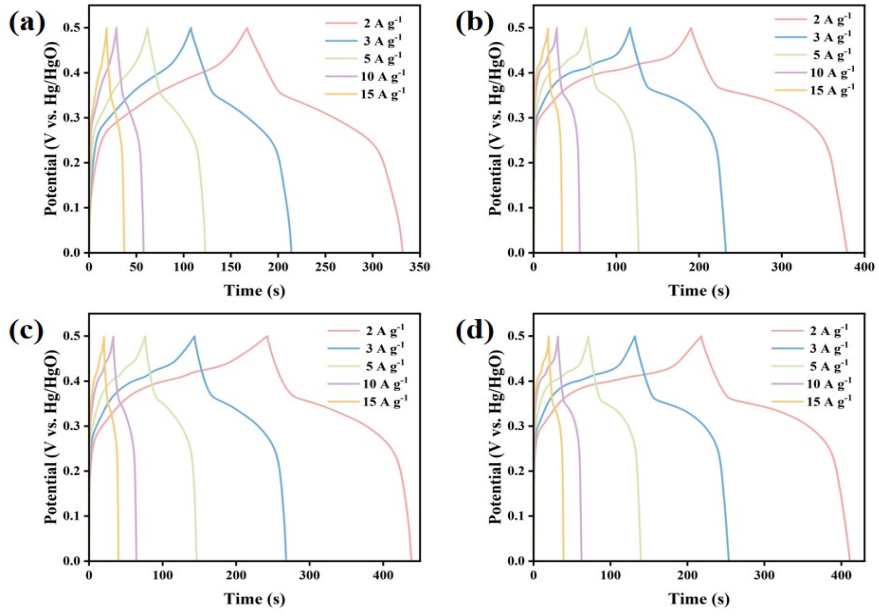

Fig. S15. GCD of the (a) ZIF-67 NCs; (b) HZIF-0.9; (c) HZIF-1.2; (d) HZIF-1.5 at different current densities.

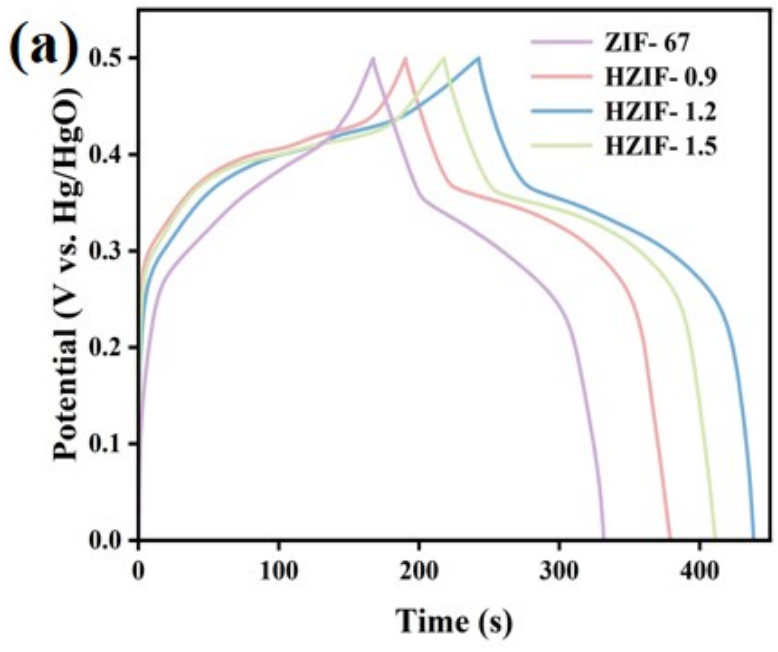

Fig. S16. Comparison of GCD curves at the current density of 2 A g^{-1}.

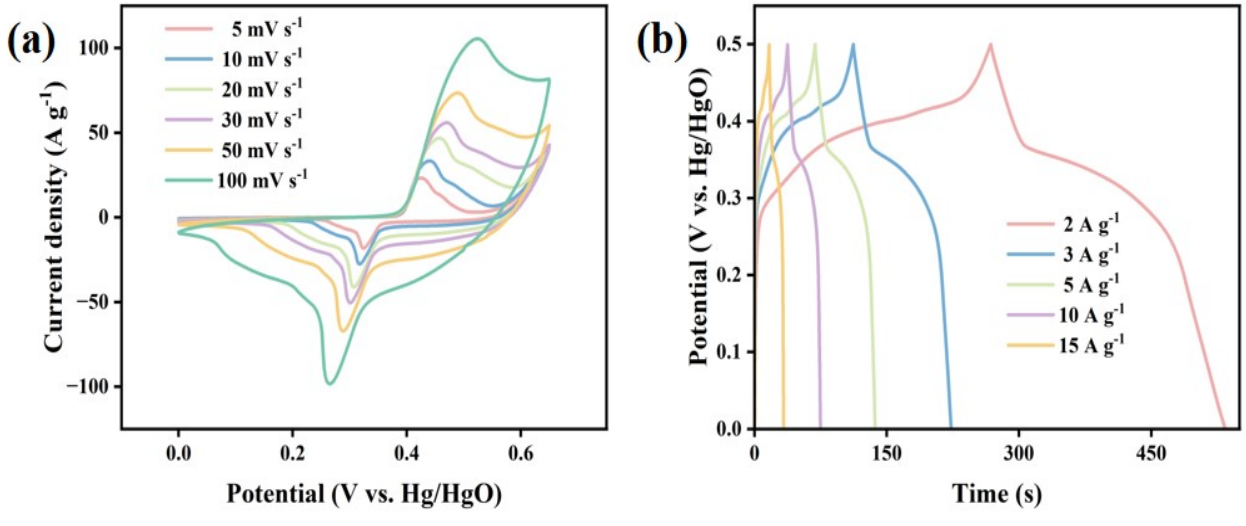

Fig. S17. (a) CV of the Co_3O_4-HNCs at different scan rates; (b) GCD of the Co_3O_4-HNCs at different current densities.

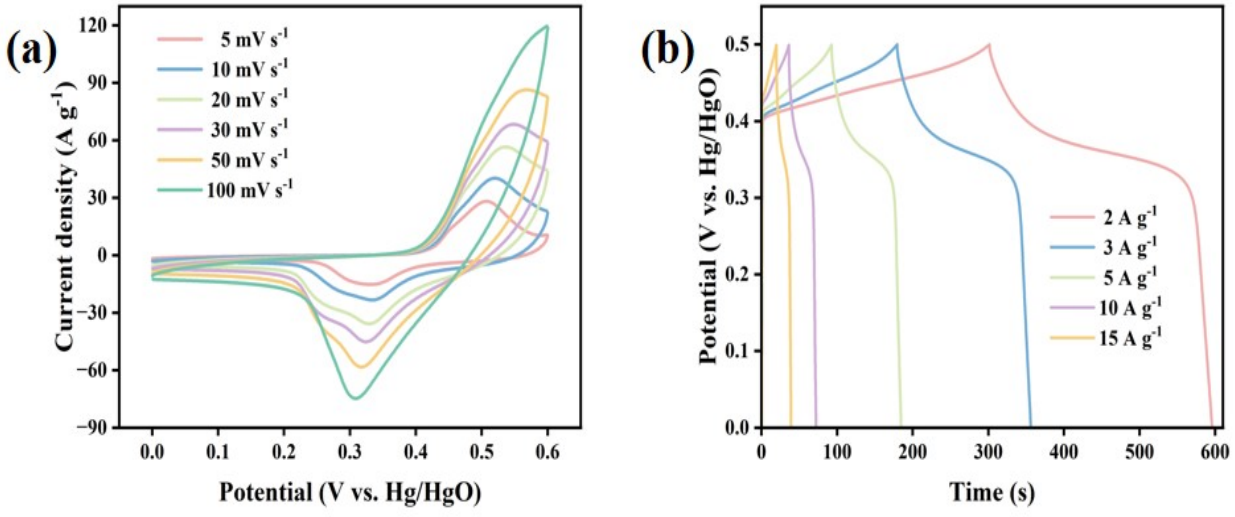

Fig. S18. (a) CV of the NiCo-LDH at different scan rates; (b) GCD of the NiCo-LDH at different current densities.

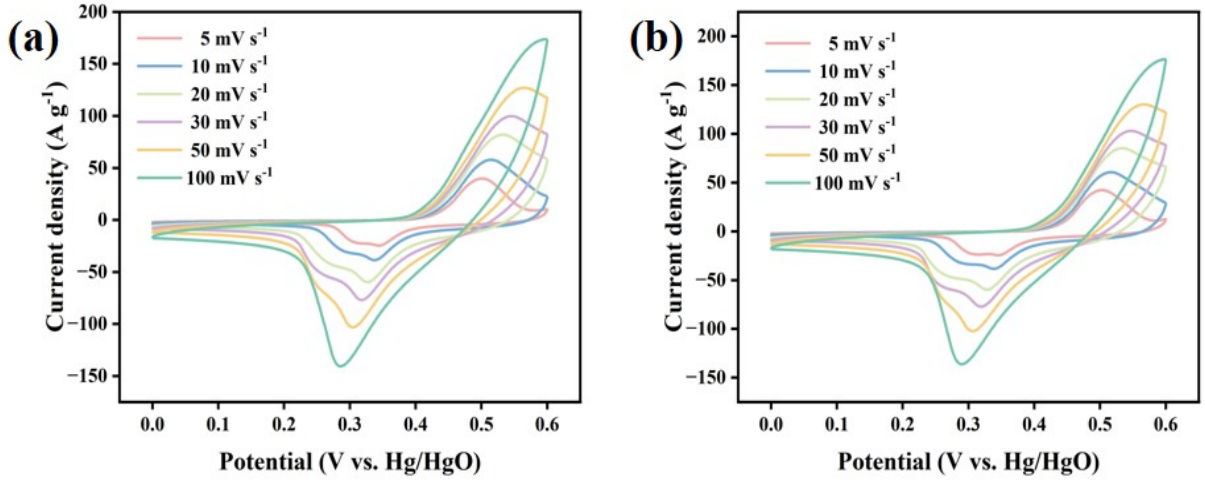

Fig. S19. CV of the (a) Co_3O_4-HNC@NiCo-LDH-0.5; (b) Co_3O_4-HNC@NiCo-LDH-2 at different scan rates.

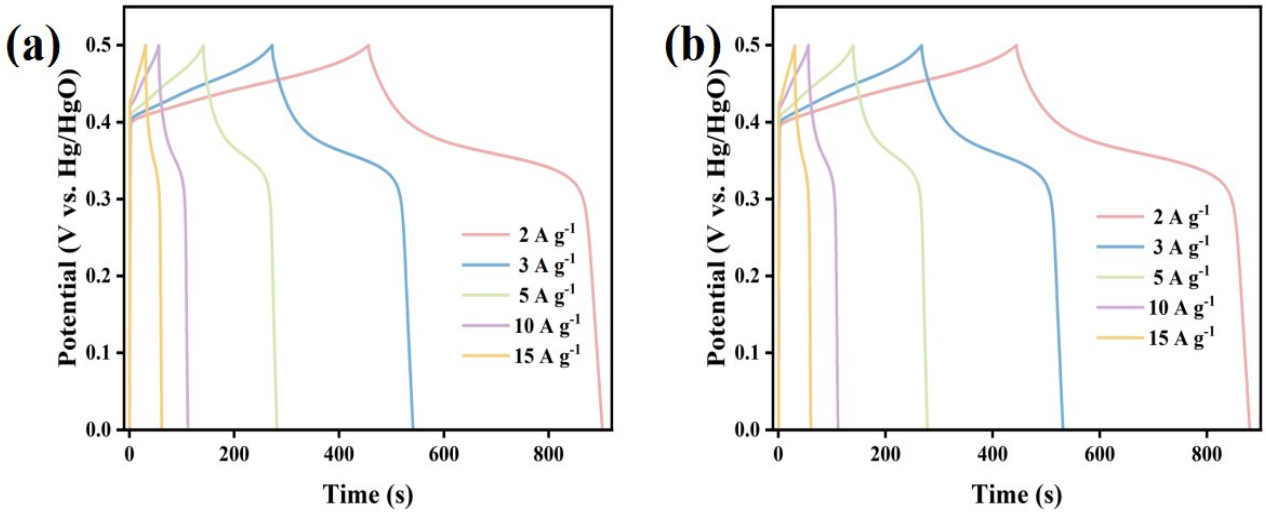

Fig. S20. GCD of the (a) Co_3O_4-HNC@NiCo-LDH-0.5; (b) Co_3O_4-HNC@NiCo-LDH-2 at different current densities.

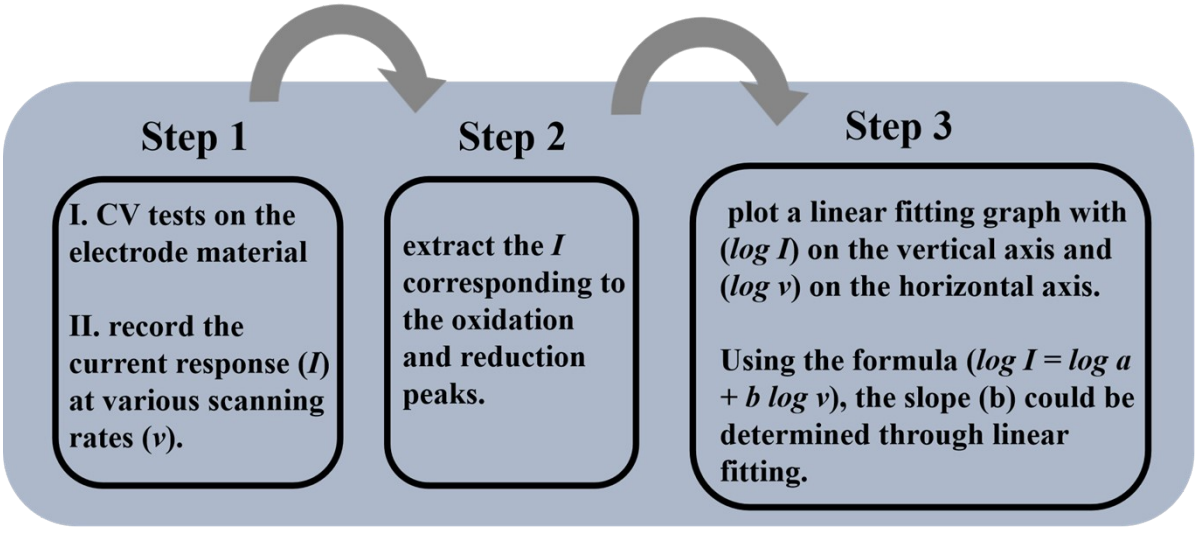

Scheme S2 A simplified diagram of the calculation process for the b value.

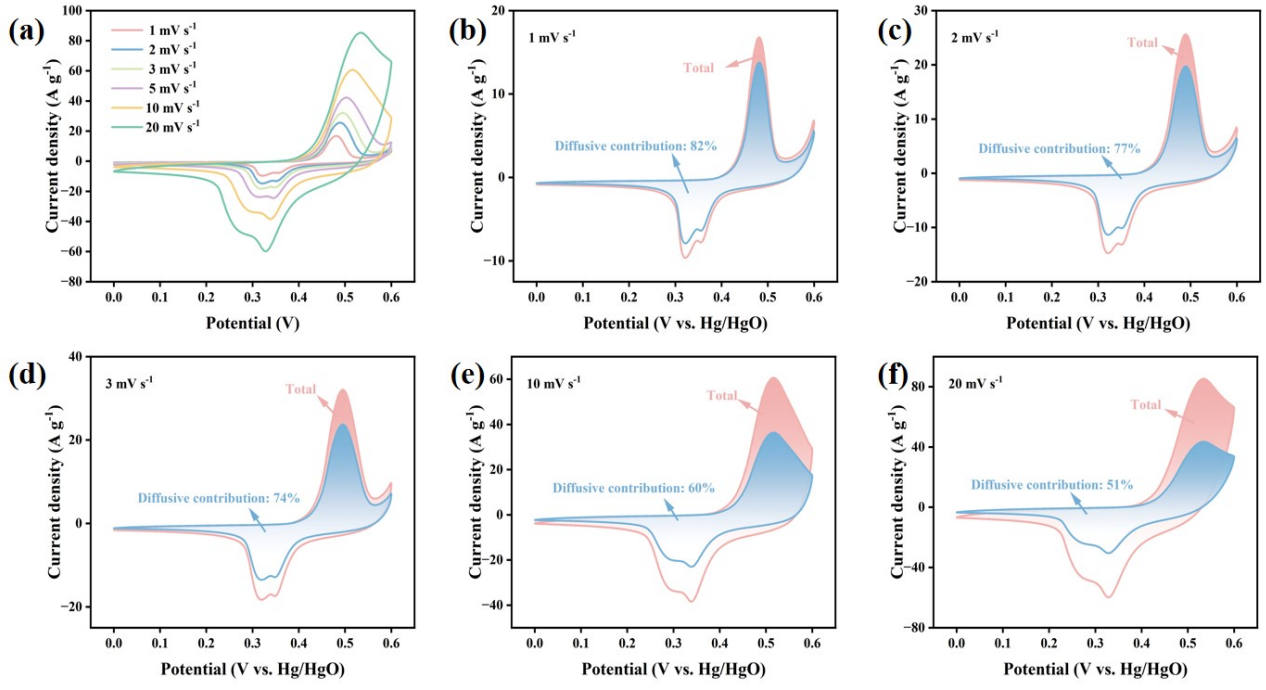

Fig. S21. (a) CV of the Co_3O_4-HNC@NiCo-LDH-1 at 1-20 mV s^{-1}; (b-f) The area proportion diagrams of diffusion control at other sweep speeds.

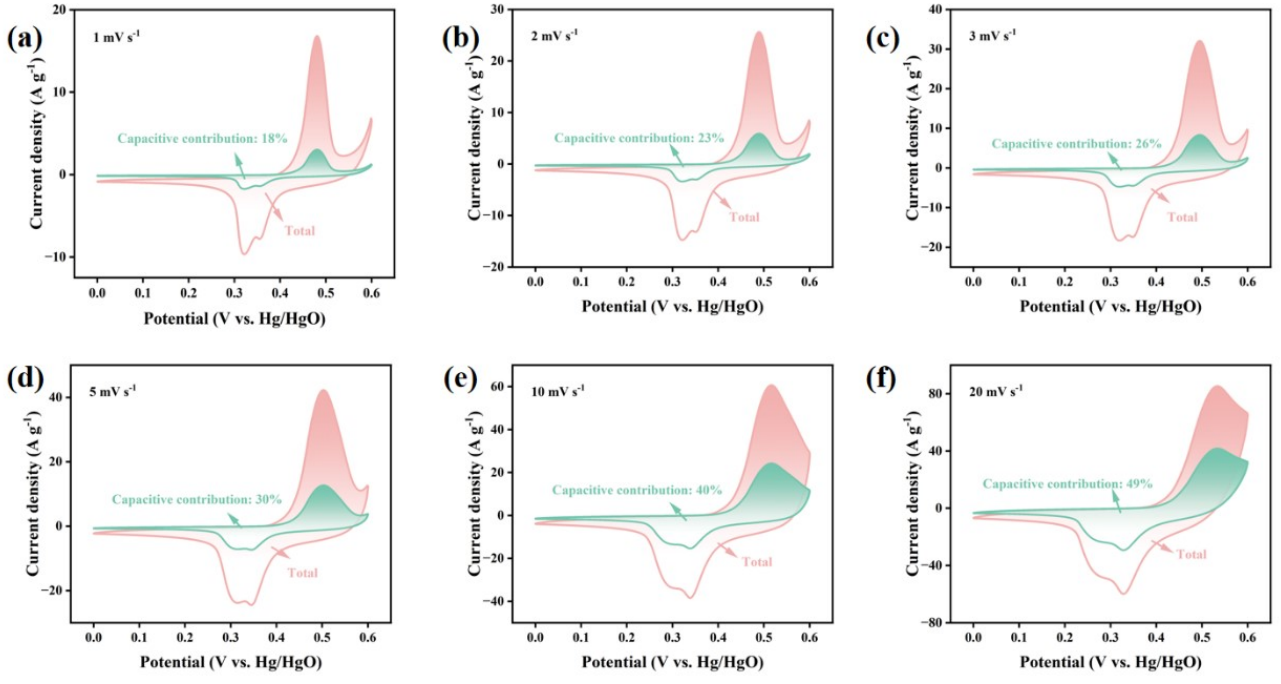

Fig. S22. (a-f) The area proportion diagrams of capacitive control at different sweep speeds.

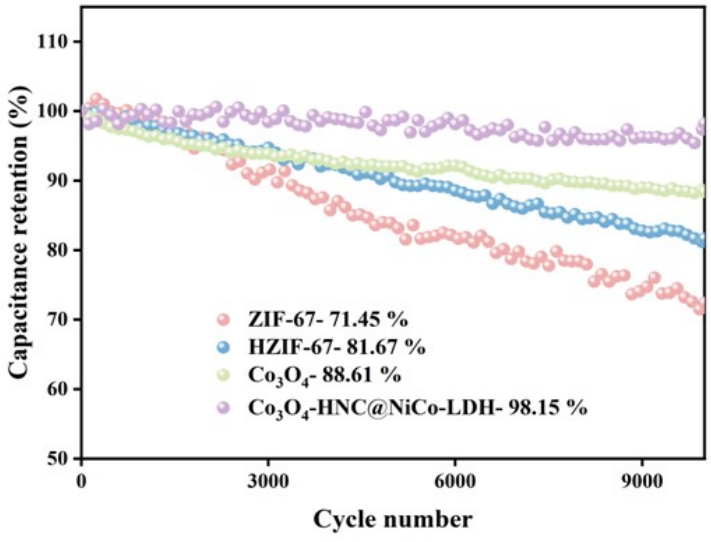

Fig.S23. Cycle performance comparison at 15A g^{-1}.

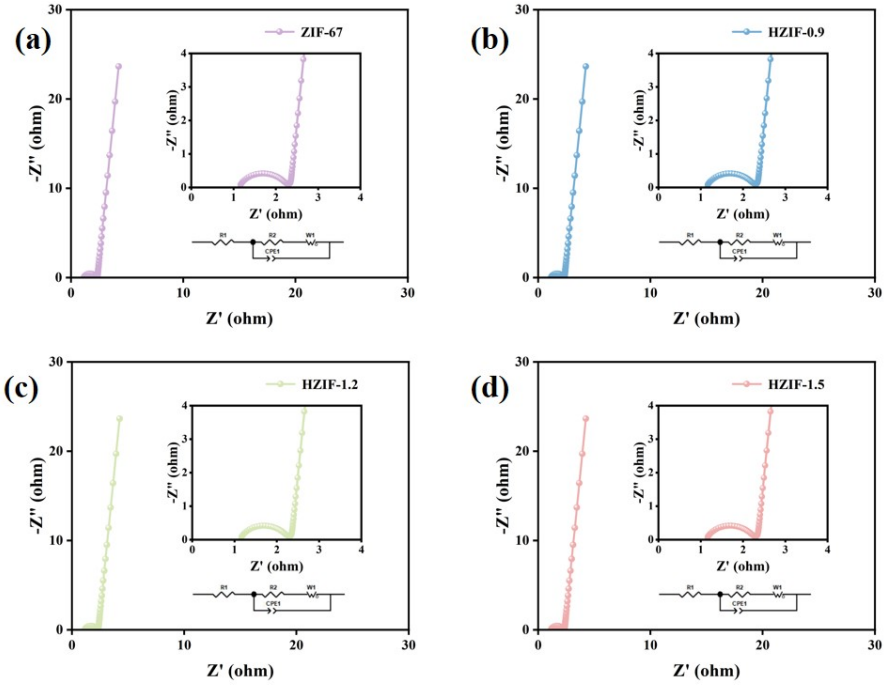

Fig. S24. Nyquist plots of (a) ZIF-67 NCs; (b) HZIF-0.9; (c) HZIF-1.2; (d) HZIF-1.5.

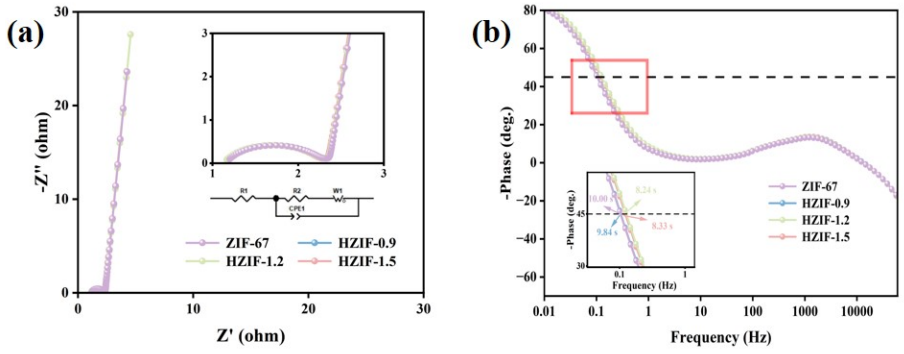

Fig. S25. ZIF and HZIF (a) Nyquist plots; (b) Bode plots of phase angle versus frequency.

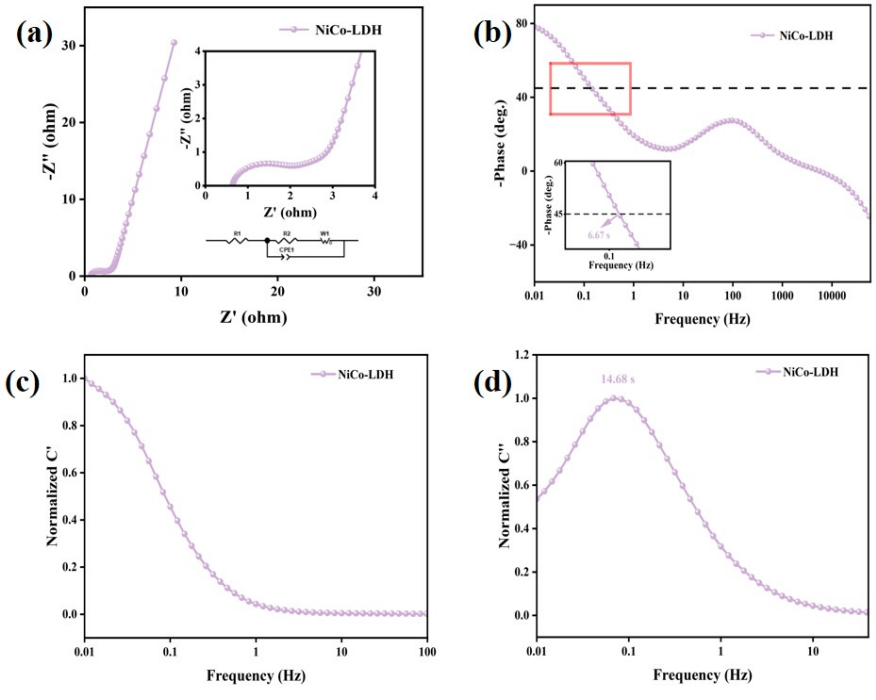

Fig. S26. NiCo-LDH (a) Nyquist plots; (b) Bode plots of phase angle versus frequency; The normalized real (c) and imaginary (d) part capacitance versus frequency.

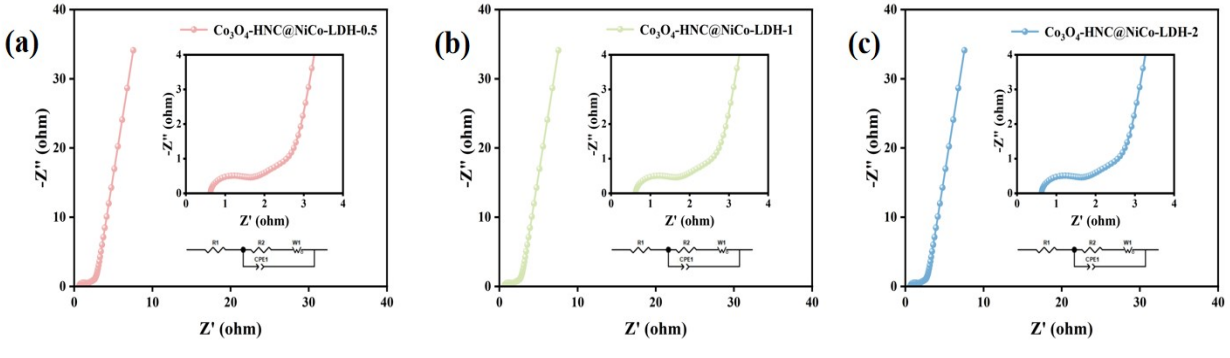

Fig. S27. Nyquist plots of (a) Co_3O_4-HNC@NiCo-LDH-0.5; (b) Co_3O_4-HNC@NiCo-LDH-1; (c) Co_3O_4-HNC@NiCo-LDH-2.

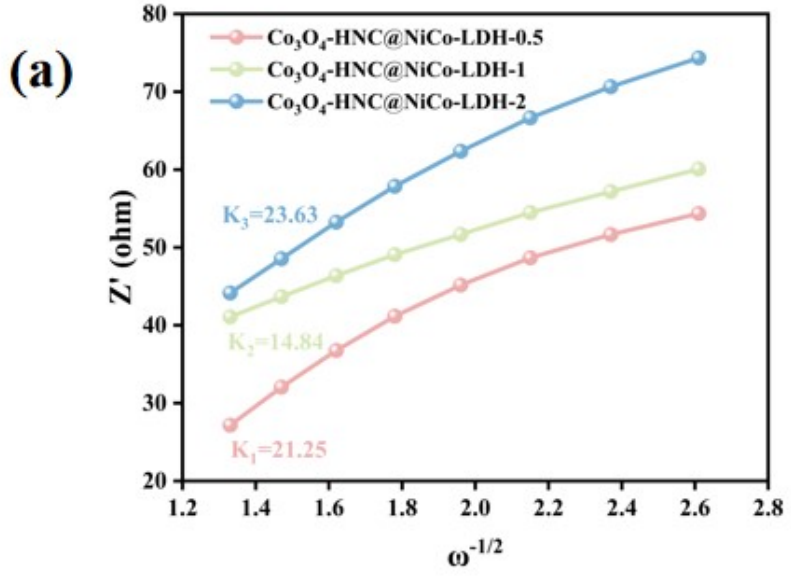

Fig. S28. Low-Frequency Warburg plots of Co_3O_4-HNC@NiMn-LDH electrodes.

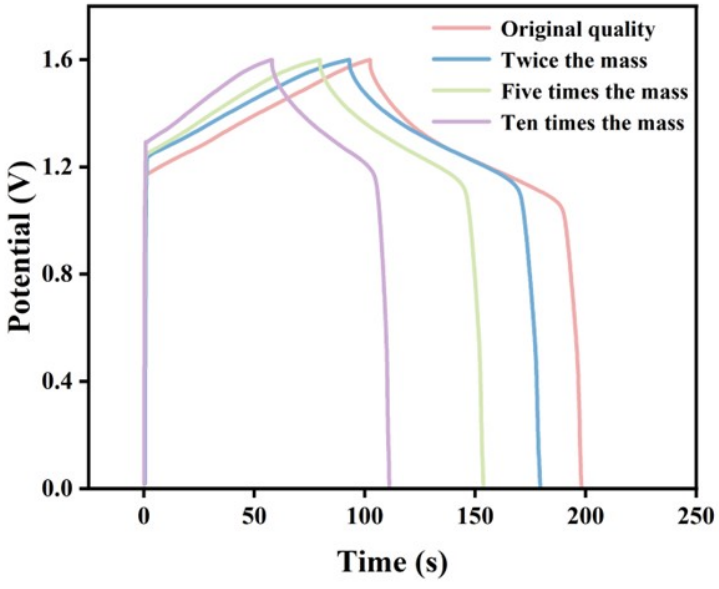

Fig. S29. High mass loading test.

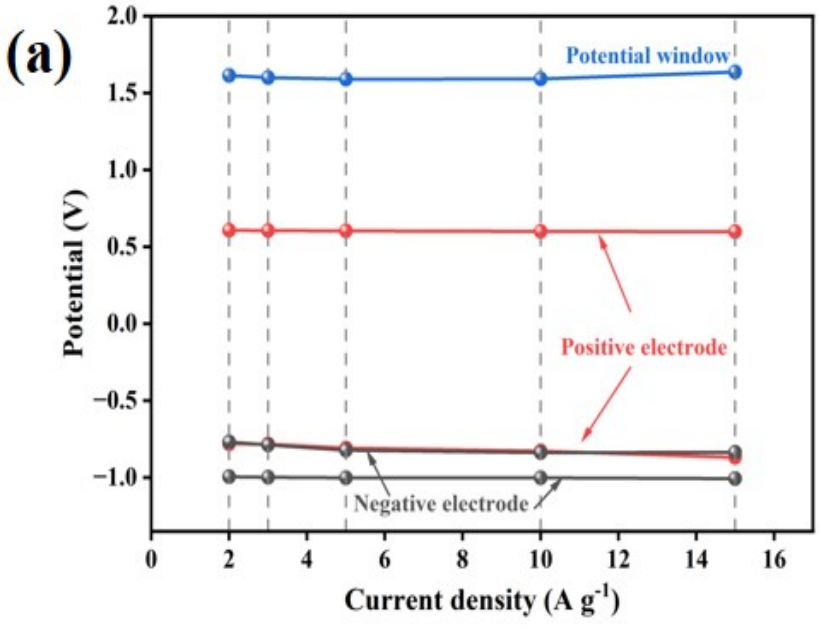

Fig. S30. The sum of the potential window provided by the positive electrode and negative material by the floating test at different current densities.

Table S1. The thickness of the LDH shell in Co_3O_4-HNC@NiCo-LDH.

Sample	Thickness of the LDH shell (nm)
Co_3O_4-HNC@NiCo-LDH-0.5	**127**
Co_3O_4-HNC@NiCo-LDH-1	**138**
Co_3O_4-HNC@NiCo-LDH-2	**162**

Table S2. The proportion of elements of Co_3O_4-HNC@NiCo-LDH-1.

Element	Series	Mass [%]	Counts	Sigma	Atom [%]
C	K-Series	45.15	18712.83	0.25	62.48
N	K-Series	5.99	4220.74	0.10	7.11
O	K-Series	21.98	21391.31	0.19	22.83
Co	K-Series	24.68	12167.19	0.37	6.96
Ni	K-Series	2.21	2095.57	0.08	0.63
Total	----------	100.00	----------	----------	100.00